

Observation of acceleration and deceleration in frontier gradient dielectric wakefield accelerators

B. D. O'Shea^{1,2}, G. Andonian¹, S. K. Barber¹, K. L. Fitzmorris¹, S. Hakimi¹, J. Harrison¹, P. D. Hoang¹, M. J. Hogan², B. Naranjo¹, O. B. Williams¹, V. Yakimenko², J. B. Rosenzweig¹

There is urgent need to develop new acceleration techniques capable of exceeding gigaelectron-volt-per-meter (GeVm⁻¹) gradients in order to enable future generations of both light sources and high energy physics experiments. To address this need, shorter wavelength (THz) accelerators based on wakefields, where an intense relativistic electron beam radiates the demanded fields directly into the accelerator structure or medium, are currently under intense investigation. This approach has yielded success in plasma media, with well over GeVm⁻¹ acceleration shown¹. Further, plasma wakefield acceleration (PWFA) has demonstrated 50% wave energy extraction efficiency². However, due to the presence of free charges and currents in contact with the beam, plasmas also introduce potentially deleterious effects not usually found in accelerators. A promising alternative, the dielectric wakefield accelerator (DWA)³ under investigation here, has shown structure breakdown accelerating field limits⁴ in excess of 5 GVm⁻¹. However, acceleration gradients in excess of 69 MeVm⁻¹ have not yet been demonstrated^{5,6,7}. In a dramatic advance, we report here measured average drive beam deceleration gradients of 1.347 ± 0.020 GeVm⁻¹ in a 15 cm long DWA, corresponding to a median energy change of over 202 ± 3 MeV in a 20.35 GeV electron beam. We further show that, when the electron bunch is divided to form a driver-witness pair, an average accelerating gradient of >320 MeVm⁻¹ is observed, with an associated wave-energy extraction efficiency of $\sim 80\%$. Moreover, such high-gradients open up research into the excitation and mitigation of undesirable higher-order dipole modes⁸. The acceleration gradients measured here, exceeding those in current accelerators by an order of magnitude, may enable, e.g., a sub-km TeV-class electron-positron collider⁹. Such a large instrument has similarities to the X-ray free-electron laser (FEL¹⁰) in the present need to construct lengthy >10 GeV¹¹ linear accelerators. As there is great demand for such sources^{12,13,14}, ways of diminishing their size and cost may significantly enhance their already revolutionary impact.

In present frontier high field linear accelerators (linacs) extremely large electromagnetic (EM) powers are needed to obtain the desired acceleration gradients. To mitigate this power demand acceleration at shorter EM wavelength, moving from the cm to the sub-mm (THz) regime, is favored. However, between radio-frequency (RF) and infrared (IR) wavelengths there is a dearth of high power sources. As such, development of new GeVm⁻¹ acceleration techniques requires fundamental rethinking of the power source. Additionally, traditional RF structures are limited by breakdown of the metallic cavity walls. Thus to support large amplitude longitudinal electric fields one must examine alternate power sources and media.

A wakefield based accelerator is a system in which an intense charged particle beam directly excites accelerating fields in a slow-wave, phase velocity $v_\phi < c$, structure or medium. This allows for the generation of large accelerating fields at wavelengths where no traditional power source exists. Here we experimentally investigate this promising means of generating and supporting GeVm⁻¹ fields using wakefield-excited dielectric tubes - the DWA.

Wakefield schemes have been investigated intensively in the context of plasmas (plasma wakefield acceleration, PWFA), in which sustained acceleration of over 40 GeVm⁻¹ in approximately one meter has been demonstrated¹. More recently, high-efficiency acceleration has been demonstrated, exceeding 50%, using a drive-witness bunch configuration². While the use of plasma permits extremely high accelerating gradients, they also introduce difficulties such as instabilities, collisions and radiative processes that are not present in today's accelerators. Plasma wakefield schemes also encounter challenges in accelerating positively charged particles¹⁵. Investigation of optical-infrared accelerators based on dielectrics (dielectric laser accelerators, DLA)¹⁶ have shown deduction of >300 MVm⁻¹ fields^{17,18} from an increase in injected beam energy spread. This recent experiment illustrates some difficulties of the DLA approach, which include breakdown-limiting fields at the \sim GVm⁻¹ level as well as production and transport of beams with unprecedented small spatial extent, given the sub- μ m apertures and wavelengths found in optical-IR DLA structures¹⁹. The THz-regime dielectric wakefield accelerator (DWA) demonstrated here addresses the above mentioned challenges in addition to offering gradients of the same order of magnitude as THz frequency plasma-based PWFA and LWFA systems. Further, given the expanded operating wavelength used in THz DWAs, transport issues associated with DLA apertures are avoided.

¹ Department of Physics and Astronomy, University of California, Los Angeles, Los Angeles, California 90095, USA, ² SLAC National Accelerator Laboratory, Menlo Park, California 94025, USA

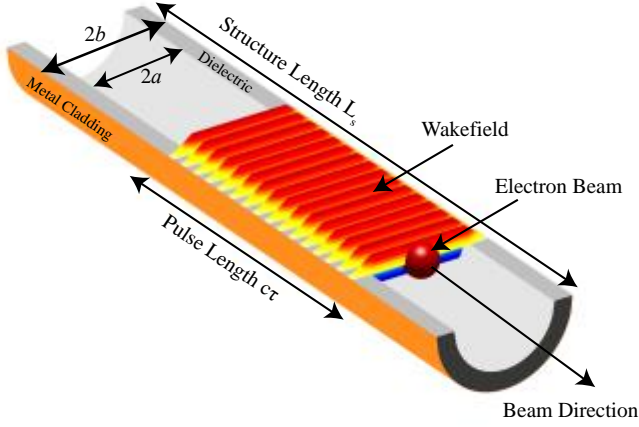


Figure 1. Graphical representation of dielectric wakefield accelerator. DWA cutaway view with the dielectric shown in gray and metal cladding in copper. The beam (dark red) travels along the structure in the vacuum region, leaving an idealized accelerating wakefield E_z shown in a color intensity map (red to blue). The wakefield inside of the excited wave-train is shown as constant in magnitude as a function of distance behind the beam, consistent with theory and simulation assuming lossless media. This is in contrast to the experimental results in Figure 4, which display dissipation effects.

As an electron beam traverses the DWA, it couples to the structure electromagnetic (EM) modes via their longitudinal electric field (E_z). Since the wakefields are excited in a dielectric material by ultra-relativistic particles the modes excited are classified as guided Cerenkov²⁰ radiation. The peak E_z associated with such a coherent Cerenkov excitation process is estimated^{4,21} as $E_z \propto eN_b/\sigma_z$, where e is the electron charge, N_b the number of beam electrons, and σ_z the rms beam length. To obtain this scaling, we assume the transverse structure inner and outer radii (a, b) used are proportional to σ_z . Emission coherence is achieved through spatial localization of the radiating electrons, *i.e.* using beams with longitudinal extent short compared to the mode wavelength λ , *i.e.* $\sigma_z < \lambda/2\pi$. For a given structure the mode frequencies are determined by the transverse boundary conditions²²; thus large E_z is obtained when higher charge eN_b and small beam dimensions ($\sigma_z, \sigma_{x,y} \ll a$) are used, where $\sigma_{x,y}$ represents the rms beam size in the two transverse directions. Such beams are available at the Facility for Advanced Accelerator Experimental Tests (FACET) at SLAC National Laboratory, where the reported experiments were performed.

The DWA structures utilized in these experiments are fabricated from SiO₂ annular capillaries coated with an outer metal layer to form dielectric lined waveguides ranging in length L_s from 1 to 15 centimeters. The structure's cylindrical symmetry, as shown in Figure 1, maximizes beam-radiation coupling. The hole in the dielectric gives a vacuum aperture that permits unobstructed near-axis beam passage.

Relevant nominal FACET beam parameters are described as follows: a 20.35 GeV electron beam consisting of approximately 2×10^{10} particles, having rms bunch length σ_z adjustable between 20 and 50 μm (peak current of 18-45 kA, see Methods) is produced at a repetition rate of 1-10 Hz. The electron beam is then focused to approximately $30 \times 30 \mu\text{m}$ rms transverse size ($\sigma_{x,y}$), with this small size maintained over tens of cm around the nominal interaction point. These beam parameters are optimum for exciting large wakefields in multi-cm length, THz DWA structures. This beam

may also be split into two components: a *driver* that excites the wakefield, and another *witness* that serves to measure the wakefield.

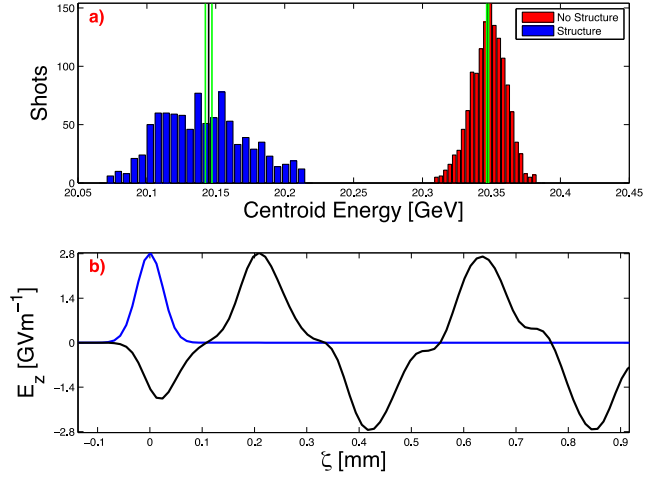


Figure 2. Measurement of large energy gradients in a DWA structure. a) Histogram of the electron beam centroid energy after traversing a 300 μm ID, 400 μm OD, 15 cm-long dielectric structure (blue, 1385 measurements) and without the structure (red, 937 measurements). Black lines mark the mean and green lines the 95% confidence intervals. The distribution resulting after beam passage through the DWA structure widens due to the parametric dependences of the energy loss. The measured average energy loss is 202 ± 3 MeV; the decelerating gradient is thus 1.347 ± 0.020 GeV/m. b) Theoretical prediction of longitudinal wake for the case of a), showing 2.8 GeV/m peak fields (normalized beam current in blue).

The primary data presented in this work is the measured changes – through acceleration and deceleration – in the beam's kinetic state after interaction with the structure. Additionally, we characterize the beam's electromagnetic interaction with the DWA by examining properties of the coherent Cerenkov radiation (CCR) generated in the structure. This combination of two types of measurement, in concert with comparisons to theoretical models, yields strong insights into GeV/m acceleration in a DWA.

We first discuss measurement of the electron beam's energy loss after traversal of a long, $L_s = 15$ cm SiO₂ capillary (300 μm ID (2a), 400 μm OD (2b)). For this particular measurement a single 20.347 \pm 0.001 GeV beam consisting of $1.929 \times 10^{10} \pm 0.003 \times 10^{10}$ electrons with a bunch length σ_z of 25 μm and a peak current $I_{\text{peak}} = 37$ kA was used. The relevant data obtained consists of the beam centroid energy, repetitively measured in a charged particle spectrometer, for several thousand shots divided between those taken with and without the structure. The result of this process (see Methods), shown in Figure 2, is the observation of an average beam energy change of 202 ± 3 MeV, corresponding to an energy gradient of 1.347 ± 0.020 GeV/m. These measurements are consistent with theory and PIC simulations, and correspond to a peak field behind the bunch of 2.8 GeV/m (Figure 2b); this is well over an order of magnitude more than the maximum used in current linacs²³. In addition, the DWA structures operated for more than 28 contiguous hours, at 10 Hz rep rate (in excess of 100k pulses) and showed no signs of deterioration in performance.

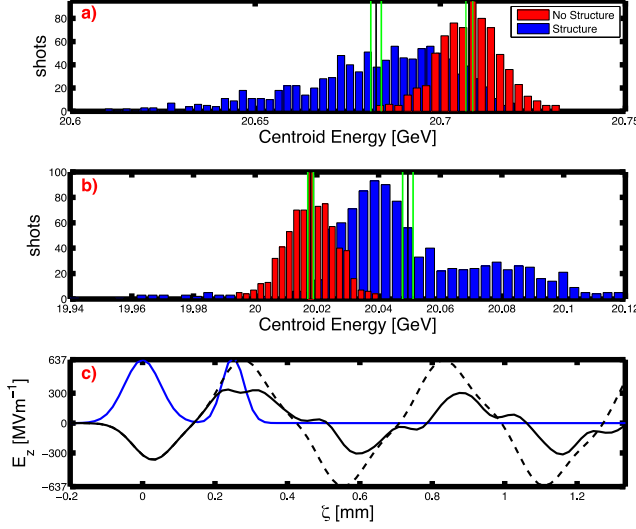


Figure 3. Measurement of accelerating gradients in a DWA structure. Histogram of centroid energy of a) the driver and b) witness bunch. Blue and red indicate measurements made with (1019 measurements) and without (722 measurements) the structure, respectively. A mean decelerating gradient of 252 ± 14 MeVm⁻¹ is observed in the driver; a mean accelerating gradient of 320 ± 17 MeVm⁻¹ is seen by the witness. c) Theoretical prediction of wake from beam current (blue), with (black) and without (dashed) witness beam.

The second phase of the experiment measured the energy transferred from a decelerating driver bunch to an accelerating witness bunch. Here, an $L_s = 10$ cm long quartz structure of 400 μm ID (2a) and 530 μm OD (2b) was used, producing a measured fundamental (TM₀₁) mode wavelength of 560 μm (See Methods). The longitudinal separation of the driver-witness pair was then optimized, using the measured TM₀₁ wavelength, to 250 μm , placing the witness slightly ahead of the peak accelerating wakefield (*cf.* Figure 3c). This placement is optimal to simultaneously obtain the highest gradient acceleration and largest efficiency. In this case, the driver and witness bunches contain $9.39 \times 10^9 \pm 0.06 \times 10^9$ and $5.94 \times 10^9 \pm 0.05 \times 10^9$ particles, with bunch lengths σ_z of 55 μm and 30 μm , respectively. The initial energy for the drive and witness bunches was 20.708 ± 0.001 GeV and 20.018 ± 0.001 GeV, respectively. The transverse beam size for both the drive and witness beam was measured as $\sigma_{x,y} = 30$ μm rms. We note that peak beam current and concomitant wake amplitude were sacrificed to produce this highly useful two-bunch structure, resulting in a drive bunch peak current of $I_{\text{peak}} = 9.7$ kA. The data set obtained, utilizing the same centroid energy change methods as the single bunch case described above, is summarized in Figure 3. We observe a driver mean decelerating gradient equivalent to 252 ± 14 MeVm⁻¹ and a mean witness bunch accelerating gradient equivalent to 320 ± 17 MeVm⁻¹. This measurement represents the largest gradient ever observed via a witness bunch in a DWA by a factor of more than four. Further, from these average energy changes, it may be inferred that the efficiency of energy extraction from the wakefield by the witness beam is $80 \pm 4\%$ - higher than demonstrated in recent PWFAs experiments². We note that for comparison with recent PWFAs experiments², we define the efficiency as the percent of energy in the excited wakefield which is transferred to the witness bunch. A high-efficiency of beam loading also, per definition, diminishes the peak accelerating wake. Indeed, in the absence of the witness bunch the wake amplitude in this case is predicted by simulation to be 640 MVm⁻¹.

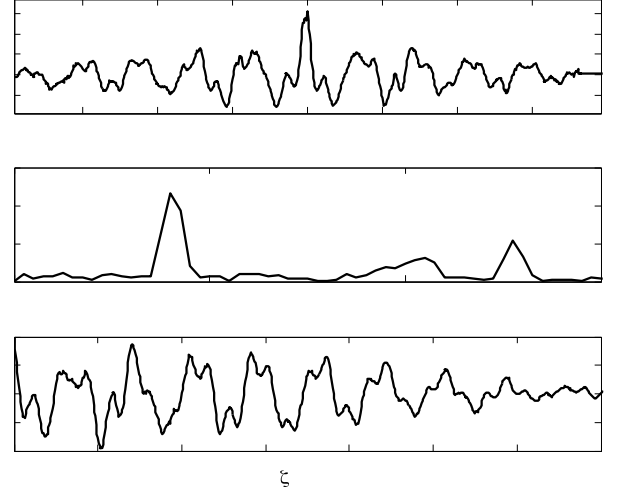


Figure 4. Modes excited in a DWA structure. a) Interferogram showing the autocorrelation of the CCR radiation generated by a single electron bunch in a 1 cm long DWA structure. The central spike is due to prompt coherent diffraction radiation generated by structure exit and collection optics. b) Spectral content of interferogram in a), with the TM₀₁ (422 GHz) and TM₀₂ (1.27 THz) modes readily identifiable. Coherent diffraction radiation gives the broad peak near 1 THz. c) Kramers-Kronig reconstruction of CCR (see Methods) in time domain from analysis of a) and b), plotted as the signal strength as a function of distance behind the driving beam, $\zeta = z - ct$.

In addition to the measurement of changes in the beam's kinetic state after passage through the DWA structure, electromagnetic properties of the radiated modes in the structure are experimentally examined. This aspect of the measurement consists of obtaining the spectrum of the CCR radiation generated in the DWA through interferometric methods. Such a study benchmarks the DWA's material and dimensional properties, and can yield information about the possible excitation of undesirable hybrid electric and magnetic (HEM) modes, which are excited when the beam and DWA are not collinear. Figure 4 shows an example of measurement of the coherent Cerenkov radiation spectrum generated in the DWA, using a single electron bunch. For this case a $L_s = 1$ cm, 450 μm inner diameter (ID, 2a), 640 μm outer diameter (OD, 2b) SiO₂ structure was employed. Excitation of the fundamental transverse magnetic TM₀₁ (at 422 GHz) and next order TM₀₂ (at 1.27 THz) modes is evident in the spectrum; the frequencies are in agreement with theoretical calculations. This measurement represents the first measurement of modes with frequencies greater than 1 THz excited in a DWA structure. The first two HEM dipole modes supported in this structure are expected near 350 and 585 GHz. The system used for positioning the DWA has a resolution of 2 μm , or a maximum angle of 40 μrad from end-to-end in a 10 cm structure, so no excitation of the HEM modes was observed.

As a consequence of the methods used in the spectral measurement, time domain information is retrievable and reveals heretofore unobserved damping effect of the radiation generated in DWAs. Assuming a lossless dielectric, the radiation pulse length exiting the structures at group velocity $\beta_g c$, where β_g is the group velocity of the mode and c the speed of light, should be proportional to L_s , as $c\tau = L_s(1 - \beta_g)/\beta_g$ (*cf.* Figure 1). For this example the group velocity of the CCR in the structure is $\beta_g = 0.39$ and the TM₀₁ bandwidth in the 1 cm structure is measured to be 14% FWHM, far exceeding the Fourier transform limit derived from the value associated with $c\tau$ of 1.8%. The observed CCR

bandwidth from the $L_s=1$ cm structure is an order of magnitude larger than that previously measured in similar structures with fields in the MVm^{-1} range excited by a 13 MeV electron beam²². When a 10 cm structure is used the bandwidth decreases to $<5\%$ FWHM; this is, however, even further from the lossless transform limit of 0.18% indicated by a CCR pulse length of 708 picoseconds.

This deviation in bandwidth from theory is due to strong damping of the wakefield as it propagates, as is suggested by inspection of the autocorrelation (Fig. 4a). To quantify this observation in the time domain we apply a Kramers-Kronig analysis²⁴. The signal reconstruction obtained (Figure 4c) maps the wakefield-derived signal with 10 fs resolution (see Methods). This wakefield measurement method represents a powerful new approach in such techniques. The reconstruction yields a signal similar to the wakefield predicted and confirmed by both theory and simulations using fully EM particle-in-cell (PIC) codes²⁵ (not shown), but with amplitude damping superimposed. The wakefield modes themselves were calculated by via direct solution of Maxwell's equations and confirmed using PIC simulation and found to be in excellent agreement. However, the observed damping in experiment is much larger than that ascribable to dielectric or metallic losses under standard conditions.

It should be emphasized that this observed damping does not impact the acceleration and deceleration studies presented in this work, as the time scale for these effects to assert themselves is >100 picoseconds, while the driver-witness beams interact with a separation of less than a picosecond. Nevertheless this damping is an expected feature — comparison with previous studies²⁴ makes it clear that the observed damping is introduced by use of a very intense, short pulse electron beam. As such the basis of this effect can be uniquely studied at FACET, which will be further investigated in the future.

The reported experiments represent a significant step forward in advanced acceleration techniques, and open the path towards exploration of critical issues in GeVm^{-1} DWA research. These include: extension of the interaction to longer structures and larger relative energy gains; excitation of HEM dipole modes in high-gradient structures and related transverse stability of driver and witness bunches in long DWAs (see Methods); experimental exploitation of CCR-derived THz; and clarification of the microscopic mechanism behind the wakefield dissipation and its implications for multi-bunch DWA operation, to name but a few. Beyond these next steps, there lay numerous avenues for development of new types of DWA structures based on dramatically different geometries, photonic mode confinement²⁷, and novel materials. Such innovations may help pave the way to application of this promising GeVm^{-1} accelerator across a broad swath of science.

Acknowledgements

The UCLA effort on this experiment has been funded by U.S. Dept. of Energy Divisions of High Energy Physics and Basic Energy Sciences under Contract Nos. DE-FG02-07ER46272, and DE-FG03-92ER40693. The SLAC effort on this experiment has been operated with funding from the United States Department of Energy contract DE-AC02-76SF00515.

Author Contributions

All authors contributed significantly to the writing of this paper.

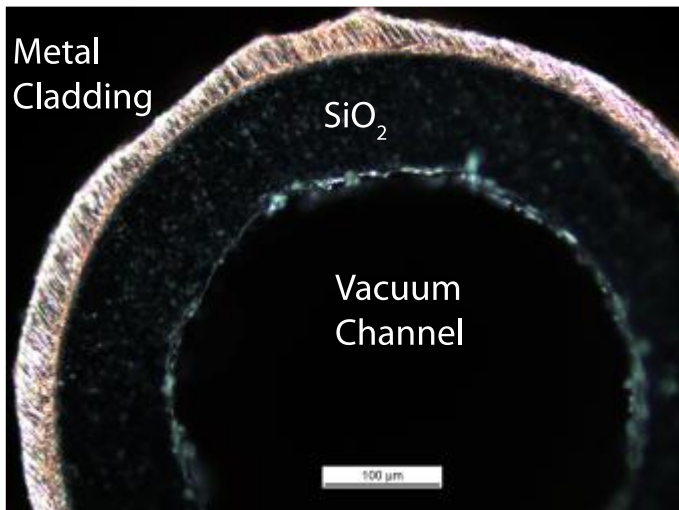
Author Information

Reprints and permissions information is available at www.nature.com/reprints. The authors declare no competing financial interests. Readers are welcome to comment on the online

version of the paper. Correspondence and requests for materials should be addressed to B.D.O. (boshea@slac.stanford.edu).

Methods

Metallic Coatings. To form the DWA structure the SiO₂ capillaries must be coated with a metal outer layer. The process of forming the coating involves first chemical cleaning the bare dielectric fibers. Following this, a 30 nm seed layer of aluminum is deposited onto the capillary using a vapor deposition system. The large electronegativity difference between the quartz and the aluminum ensures a strong covalent bond at the SiO₂-Al surface. Next, a 500 nm layer of copper is vapor deposited over the aluminum, forming a metallic bond between the two metal layers. The structures are then transferred to an electroplating bath that is used to add copper to a thickness of ~10 μm . Following the electroplating bath the structures are mounted into a holding chuck and a precision diamond saw is used to cut the structures to desired length. After cutting, the structure ends are polished using micrometer grain sandpaper and examined under a microscope for end surface finish.



Extended Figure 1. Structure photo. A high-resolution image of the end of a 400 μm ID, 530 μm OD structure. To ensure proper waveguide fabrication, images are taken of the structures prior to their installation in the experimental apparatus at FACET. Additionally, the vacuum apertures are checked by visual inspection and laser transmission techniques to ensure that they are not blocked by debris during the fabrication process.

Beam-structure alignment. The electron beam is aligned to the DWA structures using a three-step process. To establish the electron beam's vector through the experimental region, with the DWA outside the beam path, the electron beam's position on diagnostic (optical transition radiation, OTR) screens is recorded by cameras located at the interaction point (IP), upstream and downstream of the experimental chamber. Electron beam operation is ceased and a green diode laser is steered to the electron beam trajectory utilizing the diagnostic screens. The laser is focused down to simulate the electron beam's transverse dimensions in the DWA interaction region. The DWA structure is then moved into position using the green laser as a guide, thus permitting the structure to be well aligned to the beam trajectory without the electron beam impinging on the structure and avoiding possible damage.

Electron beam. The nominal beam energy is 20.35 GeV with an uncorrelated rms energy spread of $\sigma_E=298$ MeV, or 1.1% of nominal energy. A typical beam consists of approximately 2×10^{10} electrons, corresponding to 3.2 nC of total charge with repetition rate variable from 1 to 10 Hz. For this paper the current is defined

assuming a Gaussian longitudinal beam form factor, $I_{\text{peak}}=cNe/\sigma_z$. In calculation and simulation the measured parameters Ne and σ_z are used directly, leaving the definition of current as a matter of convention. The electron beam spot size at the interaction point is measured using OTR screen and wire scanner methods. The longitudinal extent of the driver and witness beams is measured using a transverse deflecting cavity². For the experiments performed in this work the rms transverse sizes σ_x and σ_y were consistently near 30x30 μm , while the bunch length σ_z was varied from 25 μm to 50 μm . In a significant extension of FACET capabilities, the longitudinal beam profile was also strongly varied using momentum dispersion in tandem with selective collimation. This technique produced the option of creating a driver and witness pair; the methods utilized are described in detail in Ref. 2.

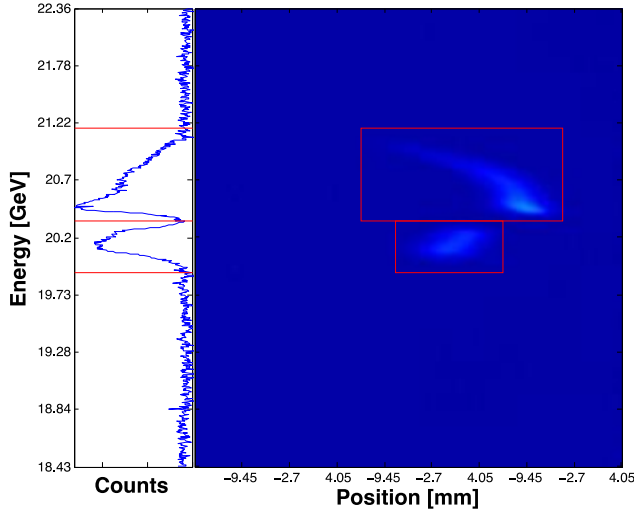
Coherent Cerenkov radiation measurements. The coherent Cerenkov radiation (CCR) that propagates downstream in the DWA tube after beam excitation exits the structure into an impedance matched launching horn having a full opening angle of 19 degrees. The CCR is then propagated quasi-optically, first encountering an off-axis paraboloid (OAP) mirror, which serves to collimate the radiation. It is directed through a polymer-based vacuum window with optimum THz transmission characteristics and reflected into a scanning Michelson interferometer equipped with pyroelectric detectors. Scans having 10 fs temporal steps, and thus equivalent resolution, are then used to create an autocorrelation-based interferogram. A fast Fourier transform (FFT) of the interferogram is performed and the spectral content of the CCR is obtained. This spectral amplitude information is further analyzed to deduce the time-domain amplitude and phase via a Kramers-Kronig reconstruction analysis²⁴, which reproduces the so-termed minimal phase consistent with the measured spectral intensity. This approach is robust for non-dispersed radiation signals, and has been shown previously to yield accurate results through benchmarking radiation profiles. Given the fixed relationship between the propagating transverse EM field measured at the interferometer and E_z within the DWA, this method gives a resulting form proportional to the time dependence of E_z for each mode at the exit of the DWA. While the amplitude relationship between the modes is not strictly preserved in this type of measurement, the method does robustly return the minimal phase, and thus the time domain wave form in this approximation, which is of central interest.

Spectrometer (energy) measurements. The spectrometer consists of a pair of quadrupole magnets, used to transversely focus the beam after the interaction point, and a dipole magnet, which is used to disperse the beam's momentum distribution. The optics of the system are set so as to provide point-to-point imaging in the dispersive direction, as well as substantial magnification of position and angle in the non-dispersive direction. After the dipole the beam passes through a vacuum-air interface and subsequently impinges on a scintillating LANE screen. The dispersed beam then passes through a pair of mirror finished silicon wafers that are 1.4 cm apart. Since the beam velocity exceeds the phase velocity of light in air, Cerenkov light is produced. This light is collected and imaged onto a 16-bit CMOS camera.

The spectrometer video imaging resolution evolved continuously due to improvements made during the two-year experimental period of the measurements here. The resolutions obtained for a static pixel size of 25 μm in various measurements ranged from 4.8 to 15.0 MeV/pixel. With the rms energy spread quoted above, the beam (full width, $6\sigma_E$) spans approximately 100 pixels. Since we are interested in a measurement of the average, or centroid, of the beam momentum (and thus energy) distribution, we are performing

a middle Riemann sum approximation to calculate the first moment of the beam's distribution function. The error in such an approximation is given by $\text{Error} \leq M_2(f-g)^3 / 24n^2$, where $(f-g)$ is the span of the integral approximated by the sum, n is the number of sub-intervals (pixels in this case) and M_2 is the maximum of the absolute value of the second derivative of the function being integrated. For these calculations we assume the energy spread is well approximated by a Gaussian distribution, and thus $M_2 = \sigma_E^2$, $(f-g) = 6\sigma_E$ and $n=100$. As a result of the single pixel resolution in the spectrometer the error in measuring the beam energy centroid is ≤ 0.2 MeV.

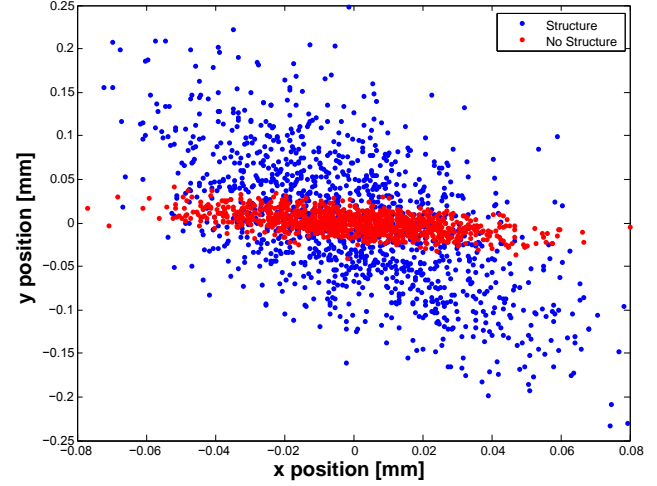
The first moment of the beam position distribution, as measured by a Beam Position Monitor (BPM) in the spectrometer transport, with and without the DWA structure present, is taken as the centroid transverse position of the beam through the spectrometer system in the non-dispersive direction (Extended Fig. 3). A linear transport model is employed to determine the absolute offset and angle of the beam at the end of the DWA structure that is due to this measured offset on the BPM when the structure is in the beam path, as compared to the nominal case without DWA present. This offset and angle is then propagated using an experimentally benchmarked beam-to-spectrometer optics model to account for any dipole induced transverse momentum that may appear as apparent longitudinal momentum (and thus energy) loss or gain in the spectrometer measurements.



Extended Figure 2. Spectrometer image. Here is shown an example of the driver (top) and witness (bottom) beams after interaction with the DWA. The red boxes indicate the ROI used for calculation of the energy and position of the beam. On the left the relative charge (represented by the counts in the pixels of the CCD camera) at each energy is shown. The limits for the ROI are again shown in red.

Histogram generation. To perform the energy loss measurements, spectrometer data is taken with and without the structure in the beam path. After alignment of the structure to the beam, the structure is inserted into and removed from the beam in periods of data acquisition lasting from 100 to 200 separate measurements. This approach reduces the possibility of fluctuations in beam energy affecting the result to an ignorable level. After data is collected each set of measurements has a region of interest (ROI) defined around the measured distribution peak to remove undue influence from background noise. In the case of the two bunch measurements, the ROI is divided into two sub-ROIs, one for the driver and one for the witness, respectively (Extended Figure 2).

The measured particle count per pixel channel at a given momentum is combined with the measured spectrometer calibration and the first moment (centroid) of the beam distribution is recorded and binned in a histogram. Once all the data for a given measurement has been obtained, the mean of the centroid is calculated and the 95% confidence interval is formed.

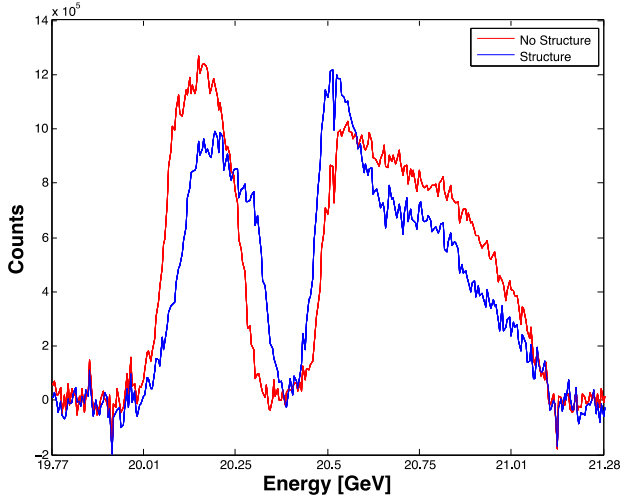


Extended Figure 3. Beam position (BPM) data after structure.

Beam position downstream of the structure location with (blue) and without (red) the structure in the beam path, as measured using a BPM in a dispersive section of the spectrometer. Here we show observed coupling to transverse modes, via a relative shift in the position of the beam. The structure parameters do not allow for an appreciable shift in beam position over the length of the interaction. As such, the measured positions are due to shifts in transverse momentum (angle) and absolute beam energy.

Dipole modes. While excitation of hybrid electric and magnetic (HEM) dipole modes supported in the DWA structures was not detected in the measured radiation spectra (*cf.* Figure 4b), the effects of these modes were observed in the beam location as found by beam position monitors (BPM) inside of the spectrometer system. The excitation of these modes are due to asymmetries in the alignment of the beam to the structure axis, specifically they arise if the beam propagates off-axis. These modes generate fields that deflect the beam in a direction perpendicular to the nominal propagation direction, and thus change the beam transverse position downstream of the DWA.

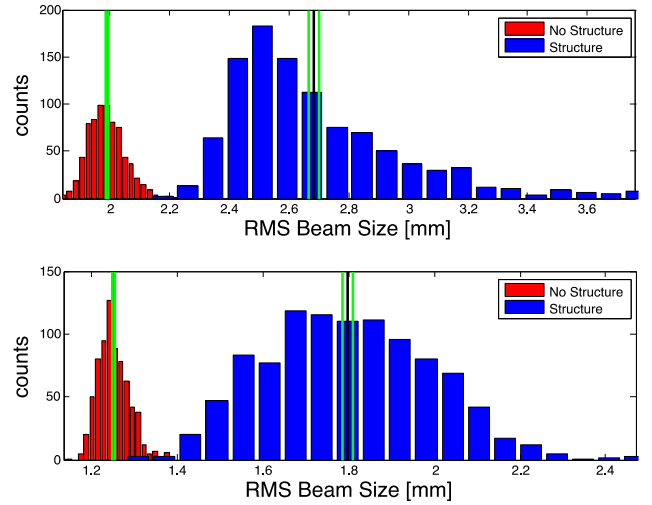
The linear transport model that is used to account for offset and angle in the measured centroid energy can be used to quantify the transverse momentum imparted to the beam as it traverses the structure. A plot of the beam position for the two-bunch experiment, shown in Extended Fig. 3, show an rms spread in position of 12 μm without the structure and 78 μm with the structure. No offset in centroid is observed. Since the bunch separation of 250 μm represents a significant fraction of the excited wavelength we attribute the change in beam position entirely to motion of the witness beam. This results in an offset of the witness beam of 169 μm , which would indicate a transverse field of 4 MV/m. In contrast, the high gradient experiment shows a change in offset, at the BPM, of 864 μm , resulting in a transverse gradient of 13.7 MV/m. Since the point at which the beam position is measured is dispersive the measured offset is not indicative of free space propagation. If the beam were allowed to propagate without a focusing system for containment the beam would move off by the width of the high gradient structure, 300 μm , in 30 m.



Extended Figure 4. Driver and witness energy spectra. The energy spectrums for the case of interaction with the DWA (blue) and no structure (red). The drive beam is on the right, while the witness beam is on the left. The energy spread for the drive beam is seen to be approximately conserved, at 1.1% prior to deceleration and 1.08% after. The energy spread of the witness beam is seen to increase from 0.44% prior to acceleration to 0.73% after acceleration.

Energy spread. For the driver-witness case the energy spread of the driver beam is found to be virtually unchanged from 1.1% in measurements without the structure to 1.08% in measurements with the structure (Extended Figure 4). The witness beam, however, is found to increase in energy spread, from 0.44% without the structure to 0.73% with the structure. The relative changes in energy spread are due to nonlinearities in the phase space prior to interaction with the structure as well as non-trivial phase curvature of the wakefields used to transfer energy between the beams. An example of the latter effect is shown in Figure 3c of the main paper in which different parts of the witness (or drive) beam can be seen to experience different gradients. This non-ideal growth in witness beam energy spread is due to the method of driver-witness beam generation. This method does not allow simultaneous control of beam current profile, driver-witness separation and shaping for ideal energy spread conservation. As the former two are necessary for proper excitation and acceleration of the witness beam, the third is constrained and thus energy spread growth is observed.

Beam Divergence. The initial divergence of the driver and witness beams, in the plane perpendicular to the dispersion induced by the spectrometer, is calculated to be 8.3×10^{-5} rad. After interaction with the structure the drive beam divergence is calculated to grow to $1.7 \times 10^{-4} \pm 1.7 \times 10^{-5}$ rad and the witness beam divergence increases to $1.35 \times 10^{-4} \pm 1.2 \times 10^{-5}$ rad. This growth is due to the aforementioned excitation of dipole modes in the structure. The excess growth of the drive beam compared to the witness beam is a consequence of the longer bunch length of the drive beam resulting in a larger sampling of the curvature of the gradients in the structure. This larger variance in longitudinal field results in a larger variance in transverse fields, and thus larger divergence changes, a consequence of the Panofsky-Wenzel theorem. This calculation is made making use of the fact that no change in the beam size is observed at the exit of the structure, so that all changes in beam size (Extended Figure 5) can be attributed to a change in the beam's divergence through transverse momentum imparted by the wakefields.



Extended Figure 5. Drive and witness beam sizes. The beam sizes of the drive (top) and witness (bottom) beams with (blue) and without (red) interaction with the structure as measured in the spectrometer. The increase in beam size is commensurate with an increase of the driver and witness beam's divergence of 100% and 61% respectively.

1
2
3
4
5
6
7
8

9
10
11
12
13
14
15

-
- ¹ Blumenfeld, I. *et al.* Energy doubling of 42 GeV electrons in a metre-scale plasma wakefield accelerator, *Nature* **445**, 741-744 (2007)
- ² Litos, M., *et al.* High-efficiency acceleration of an electron beam in a plasma wakefield accelerator. *Nature* **515**, 92-95 (2014)
- ³ Gai, W. *et al.* Experimental Demonstration of Wake-Field Effects in Dielectric Structures. *Phys. Rev. Lett.* **61**, 2756 (1988)
- ⁴ Thompson, M. C. *et al.* Breakdown Limits on Gigavolt-per-Meter Electron-Beam-Driven Wakefields in Dielectric Structures. *Phys. Rev. Lett.* **100**, 214801 (2008)
- ⁵ Gao F., *et al.* Observation of Enhanced Transformer Ratio in Collinear Wakefield Acceleration, *Phys. Rev. ST-Accel. Beams*, **11**, 041301 (2008).
- ⁶ Andonian, G. *et al.* Dielectric Wakefield Acceleration of a Relativistic Electron Beam in a Slab-Symmetric Dielectric Lined Waveguide. *Phys. Rev. Lett.* **108**, 244801 (2012)
- ⁷ Antipov, S. *et al.*, Experimental demonstration of wakefield effects in a THz planar diamond accelerating structure. *Appl. Phys. Lett.* **100**, 132910 (2012)
- ⁸ Shchegolkov, D. Yu. *et al.*, Suppressing Parasitic Effects in a Long Dielectric Wakefield Accelerator. *Proceedings of the 16th Advance Accelerators Workshop* (2014).
- ⁹ B. Barish, Nicholas Walker and Hitoshi Yamamoto. Building the Next Generation Collider. *Scientific American* (February, 2008)
- ¹⁰ Pellegrini, C., The history of X-ray free-electron lasers. *Eur. Phys. J. H* **37**, 659-708 (2012).
- ¹¹ Emma, P., *et al.* First lasing and operation of an ångstrom-wavelength free-electron laser. *Nature Photonics* **4**, 641 (2010)
- ¹² Hemsing, E., *et al.*, Coherent optical vortices from relativistic electron beams. *Nature Physics* **9**, 549 (2013)
- ¹³ Ekeberg, T., *et al.* Three-Dimensional Reconstruction of the Giant Mimivirus Particle with an X-Ray Free-Electron Laser, *Phys. Rev. Lett.* **114**, 098102 (2015)
- ¹⁴ Marinelli, A., *et al.* "High-intensity double-pulse X-ray free-electron laser, *Nature Comm.* **6**, 7369 (2015)
- ¹⁵ Yi, L., *et al.* Positron acceleration in a hollow plasma channel up to TeV regime. *Nature Sci. Reports* **4**, 4171 (2014)
- ¹⁶ England, R., *et al.*, Dielectric Laser Accelerators. *Rev. Mod. Phys.* **86**, 1337 (2014)
- ¹⁷ Peralta, E. A., *et al.* Demonstration of electron acceleration in a laser-driven dielectric microstructure. *Nature* **503**, 91-94 (2013)
- ¹⁸ Bruer, J. and Hommelhoff, P., *Phys. Rev. Lett.*, **111**, 134803 (2013)
- ¹⁹ Naranjo, B., Valloni, A., Putterman, S., and Rosenzweig, J. B. Stable Charged-Particle Acceleration and Focusing in a Laser Accelerator Using Spatial Harmonics. *Phys. Rev. Lett.* **109**, 164803 (2012)
- ²⁰ Cerenkov, P. A. Visible Radiation Produced by Electrons Moving in a Medium with Velocities Exceeding that of Light. *Phys. Rev.* **52**, 378 (1937)
- ²¹ Rosenzweig, J., Barov, N., Thompson, M., Yoder, R. Energy loss of a high-charge bunched electron beam in plasma: Simulations, Scaling, and Accelerating Wakefields. *Phys. Rev. ST Accel. Beams* **7**, 061302 (2004)
- ²² Cook, A. M., *et al.* Observation of Narrow-Band Terahertz Coherent Cherenkov Radiation from a Cylindrical Dielectric-Lined Waveguide. *Phys. Rev. Lett.* **103**, 095003 (2009)
- ²³ T. Inagaki, *et al.* "High-gradient C-band linac for a compact x-ray free-electron laser facility." *Phys. Rev. ST-Accel. Beams* **17**, 080702 (2014)
- ²⁴ Lai, R., and Sievers, A. J., Phase problem associated with the determination of the longitudinal shape of a charged particle bunch from its coherent far-ir spectrum. *Phys. Rev. E* **52**, 4576 (1995)
- ²⁵ Nieter, C. and Cary J. R. VORPAL: a versatile plasma simulation code. *J. of Comp. Phys.*, **96**, 448-473 (2004)
- ²⁷ Andonian, G., *et al.* Planar-Dielectric-Wakefield Accelerator Structure Using Bragg-Reflector Boundaries. *Phys. Rev. Lett.* **113**, 264801 (2014)